

# Online Research @ Cardiff

This is an Open Access document downloaded from ORCA, Cardiff University's institutional repository: <https://orca.cardiff.ac.uk/id/eprint/141639/>

This is the author's version of a work that was submitted to / accepted for publication.

Citation for final published version:

Mikhaylov, Roman, Stringer Martin, Mercedes, Dumcius, Povilas, Wang, Hanlin, Wu, Fangda, Zhang, Xiaoyan, Alghamdi, Fahad, Akhimien, Victory, Sun, Chao, Clayton, Aled ORCID: <https://orcid.org/0000-0002-3087-9226>, Fu, Yong Qing (Richard), Ye, Lin ORCID: <https://orcid.org/0000-0002-0303-2409>, Dong, Zhiqiang and Yang, Xin ORCID: <https://orcid.org/0000-0002-8429-7598> 2021. A reconfigurable and portable acoustofluidic system based on flexible printed circuit board for the manipulation of microspheres. Journal of Micromechanics and Microengineering 31 (7) , 074003. 10.1088/1361-6439/ac0515 file

Publishers page: <http://dx.doi.org/10.1088/1361-6439/ac0515>  
<<http://dx.doi.org/10.1088/1361-6439/ac0515>>

Please note:

Changes made as a result of publishing processes such as copy-editing, formatting and page numbers may not be reflected in this version. For the definitive version of this publication, please refer to the published source. You are advised to consult the publisher's version if you wish to cite this paper.

This version is being made available in accordance with publisher policies.

See

<http://orca.cf.ac.uk/policies.html> for usage policies. Copyright and moral rights for publications made available in ORCA are retained by the copyright holders.



ACCEPTED MANUSCRIPT • OPEN ACCESS

# A Reconfigurable and Portable Acoustofluidic System Based on Flexible Printed Circuit Board for the Manipulation of Microspheres

To cite this article before publication: Roman Mikhaylov *et al* 2021 *J. Micromech. Microeng.* in press <https://doi.org/10.1088/1361-6439/ac0515>

## Manuscript version: Accepted Manuscript

Accepted Manuscript is “the version of the article accepted for publication including all changes made as a result of the peer review process, and which may also include the addition to the article by IOP Publishing of a header, an article ID, a cover sheet and/or an ‘Accepted Manuscript’ watermark, but excluding any other editing, typesetting or other changes made by IOP Publishing and/or its licensors”

This Accepted Manuscript is © 2021 The Author(s). Published by IOP Publishing Ltd..

As the Version of Record of this article is going to be / has been published on a gold open access basis under a CC BY 3.0 licence, this Accepted Manuscript is available for reuse under a CC BY 3.0 licence immediately.

Everyone is permitted to use all or part of the original content in this article, provided that they adhere to all the terms of the licence <https://creativecommons.org/licenses/by/3.0>

Although reasonable endeavours have been taken to obtain all necessary permissions from third parties to include their copyrighted content within this article, their full citation and copyright line may not be present in this Accepted Manuscript version. Before using any content from this article, please refer to the Version of Record on IOPscience once published for full citation and copyright details, as permissions may be required. All third party content is fully copyright protected and is not published on a gold open access basis under a CC BY licence, unless that is specifically stated in the figure caption in the Version of Record.

View the [article online](#) for updates and enhancements.

**A Reconfigurable and Portable Acoustofluidic System Based on Flexible Printed Circuit Board for the Manipulation of Microspheres**

Roman Mikhaylov<sup>1</sup>, Mercedes Stringer Martin<sup>1</sup>, Povilas Dumcius<sup>1</sup>, Hanlin Wang<sup>1</sup>, Fangda Wu<sup>1</sup>, Xiaoyan Zhang<sup>2</sup>, Fahad Alghamdi<sup>1</sup>, Victory Akhimien<sup>1</sup>, Chao Sun<sup>3</sup>, Aled Clayton<sup>4</sup>, Yongqing Fu<sup>5</sup>, Lin Ye<sup>6</sup>, Zhiqiang Dong<sup>7</sup>, and Xin Yang<sup>1</sup>

<sup>1</sup> Department of Electrical and Electronic Engineering, School of Engineering, Cardiff University, Cardiff CF24 3AA, UK

<sup>2</sup> International Joint Laboratory of Biomedicine and Engineering, Huazhong Agricultural University and Cardiff University, Wuhan, Hubei, 430070, China

<sup>3</sup> School of Life Sciences, Northwestern Polytechnical University, 710072, P.R. China

<sup>4</sup> Tissue Micro-Environment Group, Division of Cancer & Genetics, School of Medicine, Cardiff University, Cardiff CF14 4XN, UK

<sup>5</sup> Faculty of Engineering and Environment, Northumbria University, Newcastle Upon Tyne, Newcastle NE1 8ST, UK

<sup>6</sup> Cardiff China Medical Research Collaborative, Division of Cancer & Genetics, Cardiff University School of Medicine, Cardiff, CF14 4XN, UK

<sup>7</sup> College of Biomedicine and Health, College of Life Science and Technology, Huazhong Agricultural University, Wuhan, Hubei, 430070, China

Corresponding author: Xin Yang

## Abstract

Acoustofluidic devices based on surface acoustic waves (SAWs) have been widely applied in biomedical research for the manipulation and separation of cells. In this work, we develop an accessible manufacturing process to fabricate an acoustofluidic device consisting of a SAW interdigital transducer (IDT) and a polydimethylsiloxane (PDMS) microchannel. The IDT is manufactured using a flexible printed circuit board (FPCB) pre-patterned with interdigital electrodes (IDEs) that is mechanically coupled with a piezoelectric substrate. A new microchannel moulding technique is realised by 3D printing on glass slides and is demonstrated by constructing the microchannel for the acoustofluidic device. The flexible clamping mechanism, used to construct the device, allows the reconfigurable binding between the IDT and the microchannel. This unique construction makes the acoustofluidic device capable of adjusting the angle between the microchannel and the SAW propagation, without refabrication, via either rotating the IDT or the microchannel. The angle adjustment is demonstrated by setting the polystyrene microsphere aggregation angle to  $-5^\circ$ ,  $0^\circ$ ,  $6^\circ$ , and  $15^\circ$ . Acoustic energy density measurements demonstrate the velocity of microsphere aggregation in the device can be accurately controlled by the input power. The manufacturing process has the advantages of reconfigurability and rapid-prototyping to facilitate preparing acoustofluidic devices for wider applications.

## Introduction

Acoustofluidic devices have attracted great interest in label-free manipulations of micro-<sup>1</sup> and nano- particles<sup>2</sup> owing to their considerable biocompatibility and precision. They have been demonstrated in biomedical applications for separation (exosomes<sup>3-5</sup>, tumour<sup>6</sup>, and inflammatory<sup>7</sup> cells), manipulation (cell interaction<sup>8</sup>, single cells<sup>9</sup>, and *Caenorhabditis elegans*<sup>10</sup>), and stimulation of cells<sup>11</sup>.

Surface acoustic wave (SAW) devices are almost independent from the microchannel material in terms of acoustic properties compared to bulk acoustic wave devices<sup>12</sup>. This feature makes them easy to fabricate for high-frequency applications (MHz-GHz)<sup>3,13</sup> and integrate with other systems, such as microfluidics. SAW devices are conventionally fabricated by patterning interdigital transducers (IDTs) on a piezoelectric substrate<sup>14</sup>, which convert radio frequency (RF) signals into SAWs propagating on the surface of the substrate. When the SAW meets a liquid medium, it diffracts into the medium and generates a time-averaged pressure distribution that can be utilised to precisely manipulate micro-objects<sup>15</sup>. Standing SAW (SSAW) devices, constructed by a pair of opposite IDTs working on the same frequency, are primarily used in acoustofluidic applications<sup>16</sup>. A great diversity of manipulation and actuation can be achieved by setting up the IDT structure to create, for example, tilted-angle SSAW devices<sup>17,18</sup> and 2D- and 3D-patterning tweezers<sup>8,19-21</sup>. However, IDTs manufactured through conventional techniques, such as photolithography, are permanently patterned on the piezoelectric substrate. Polydimethylsiloxane (PDMS) microchannels, used to accommodate biological samples in acoustofluidic systems, also use the photolithography process involving cleanroom facilities. Thus, acoustofluidic devices capable of manufacturing and reconfiguring in general laboratories, using off-the-shelf components, are highly desired.

A new fabrication technique, developed by our group, has successfully fabricated the IDTs without the use of a cleanroom for the manipulation of microparticles and cancer cells<sup>22</sup>. The IDTs were manufactured by mechanically clamping a rigid printed circuit board (PCB) pre-patterned with interdigital electrodes (IDEs) onto a piezoelectric substrate. This technique has been

89 benchmarked against a device made by conventional photolithography in terms of frequency  
90 response, droplet transportation, and cell manipulation. The PCB-based IDT has the advantage of  
91 replacing piezoelectric substrates by simply disassembling the mechanically clamped structure,  
92 with no need to remanufacture the IDT. Another IDT made by flexible PCB (FPCB) pre-patterned  
93 with IDEs demonstrated similar performance with advantages of dynamic flexing, less weight, and  
94 better heat dissipation<sup>23</sup>.

95 A development process with low requirement on facilities and operation of the device using a  
96 portable control unit can better support broadening the use of the acoustofluidic devices. Herein,  
97 we present a novel development technique for both the IDTs and the microchannel, we call it  
98 Versatile Acoustofluidic Device (VAD). We also demonstrate the rapid-prototyping and  
99 reconfigurability of VAD for precise manipulation of micro-objects.

## 100 **Methods and Materials**

### 101 **FPCBs**

102 The FPCB pre-patterned with IDEs, used in the VAD, was externally manufactured  
103 (circuitfly.com) using a standard PCB manufacturing process. The IDEs were made of metal  
104 bilayers (Au/Ni, 30 nm/2  $\mu$ m) patterned on a 70  $\mu$ m thick polyester laminate. The IDEs consist of  
105 40 pairs of 10 mm long finger electrodes and have a centre-to-centre finger pitch of 200  $\mu$ m as  
106 shown in Fig. 1A. The ratio between the finger spacing and finger width is 1:1. A 128° Y-cut 3-  
107 inch lithium niobate (LiNbO<sub>3</sub>) was used as the piezoelectric substrate. The VAD had a Rayleigh  
108 mode frequency of ~19.9 MHz and a 200  $\mu$ m wavelength. Two coaxial cables were soldered to  
109 the buspads of each FPCB IDEs. Matching networks (MNs) based on an LC circuit are used (Fig.  
110 1B), which are essential in reducing the impedance mismatching between the VAD and the driving  
111 power amplifiers<sup>22,23</sup>.

### 113 **Clamping Mechanism**

114 The VAD required a mechanical jig to hold the main components together, including the FPCB  
115 IDEs and LiNbO<sub>3</sub> substrate. As shown in Fig. 1C, the VAD uses a simple clamping mechanism  
116 and consists of the following stacking order from the bottom to the top: heatsink (supports the  
117 entire device and dissipates heat), temperature sensors (measure the IDT temperature), LiNbO<sub>3</sub>  
118 (produces SAWs), FPCB IDEs (convert RF to SAWs), silicon pads (evenly distribute the clamping  
119 force), localised pressers (apply the clamping force), force-sensitive resistors (FSRs) (measure the  
120 clamping force), FSR roofs (hold and press the FSRs), M5 screws (generate the clamping force)  
121 and main holders (hold the whole structure onto the heatsink). Another structure, which consists  
122 of an acrylic presser and a microchannel presser, is developed to hold the microchannel between  
123 the two IDTs. The FSR roofs, localised pressers, microchannel pressers, and main holders were all  
124 3D printed using a 0.4 mm nozzle and polylactic acid (PLA) filaments.

### 126 **The VAD Assembly**

127 The FPCB IDEs, microchannel and LiNbO<sub>3</sub> substrate were thoroughly cleaned using isopropyl  
128 alcohol and de-ionised (DI) water, dried using a compressed air duster and checked under the  
129 microscope to ensure that no fibres or dust particles were present on the parts before the final  
130 assembly. All the individual components, shown in Fig. 1C, are placed on the LiNbO<sub>3</sub> which is  
131 mounted on the heatsink. A clamping force is created by fastening the two M5 screws on top of  
132 the localised pressers. A vector network analyser (VNA) is used to monitor the reflection

coefficient ( $S_{11}$ ) and to confirm when the contact resistance is overcome and an optimal clamping force is achieved<sup>22,23</sup>. Fig. 1D shows the final assembled VAD with a portable control unit and an inset to demonstrate the full assembly including the microchannel on the heatsink.

### Microchannels

The use of a glass-bottom 3D printed mould to prepare the microchannels stands as a novelty for microchannel manufacturing, with the development flow illustrated in Fig. 2A. (1) A glass slide (76 mm (W) × 26 mm (L)) is placed on the 3D printer table and held in place using masking tape. A compensatory offset is applied by using a “Z offset setting” plugin in the 3D printer software. Glass slides with various thicknesses can be used as the glass-bottom of the mould by adjusting the offset setting. The 3D printed mould, designed in Solidworks, is directly printed on the glass slide, (2) removed from the 3D printer table after completion and left to cool. (3) The glass-bottom 3D printed mould is then placed in a plastic petri dish and filled with PDMS (Sylgard 184, Farnell UK), which is prepared according to the manufacturer’s protocol. The dish is placed onto a hot plate (SD160, Colepalmer) at a temperature of 45 °C to cure for 24 hours, which is below the 60 °C melting temperature of the PLA. (4) The set PDMS is removed from the mould, (5) the outer perimeter of the channel is cut and (6) a premade acrylic presser, with the dimensions of 47 mm (L) × 15 mm (W) × 3 mm (H), is placed on top of the microchannel. (7) The microchannel is then bolted onto the pre-assembled VAD using a microchannel presser (Fig. 2B). (8) The M5 nuts on the far edges of the microchannel presser are fastened until resistance is felt and (9) finally the M3 screws are screwed in to ensure even distribution of the pressing force.

The walls of the microchannel presser (Fig. 2A, step 9 and Fig. 2B) are created to resist excessive force and prevent it from overbending. These help to keep the force evenly distributed across the microchannel and not to over compress it. To further prevent deformation, the ratio between the PDMS and the microchannel height was 55:1.

Two examples of the glass-bottom 3D printed moulds are shown in Fig. 2C, which are single inlet/outlet and 3-inlet-2-outlet structures, respectively. Five 3D printed moulds were printed on the same glass slide and measured using a microscope to determine the repeatability of the print.

### Control Unit

To increase the portability of the acoustofluidic system and facilitate on-demand use of the VAD, a portable control unit that includes a waveform generator, a power amplifier, a microcontroller, sensors, a display, and a power supply is developed (Fig. 3).

### Coating and Sample Preparation

The microchannels were all coated with 1% (w/w) bovine serum albumin solution for 10 min and then flushed with DI water. For the microsphere test, 10 µm polystyrene microspheres (Sigma Aldrich) were used and suspended in a 23% (v/v) glycerol and phosphate-buffered saline solution. The microsphere suspension was injected into the microchannels through a syringe.

### IDT Alignment Setup and Analysis

The formation of SSAW relies on the alignment of the two IDTs, which can be reflected by the device’s insertion loss ( $S_{21}$ ). The smaller the insertion loss, the better the SAW transmission from one IDT to another. Thus, one can effectively use the VNA to estimate the IDT alignment. This is demonstrated by connecting two IDTs to the VNA as a two-port network, as shown in Fig 4. The test keeps one of the IDTs unmoved, as the receiving IDT, while rotating the other IDT, as the

transmitting IDT. The  $S_{11}$  of the transmitting IDT is measured during this procedure to monitor how it changes with the rotation. Top view images of the transmitting IDT at different orientations were captured by an overhead camera, which were then analysed using a customised MATLAB code that extracted the angle between the two IDTs. Five reference angles,  $17^\circ$ ,  $11^\circ$ ,  $6^\circ$ ,  $2^\circ$ , and  $0^\circ$ , were determined for the  $S_{21}$  readings, which were selected by finding the most observable change in the  $S_{21}$ .

**Acoustic Energy Density Analysis**

To characterise the acoustic energy density inside the VAD, a MATLAB code adapted from Barnkob et al<sup>24</sup> was applied to analyse the trajectory of microspheres. In short, image frames extracted from microscope-captured movies, during the microsphere aggregation process, were analysed for pixel intensity near the pressure node (PN) line. The last frame of each movie was used as the maximum intensity frame. The normalised intensity and the relative intensity of each middle-process frames were then calculated and fit into an expression using a fitting parameter.

**Results and Discussion**

**IDT Alignment**

Compared to cleanroom made SSAW devices, the VAD depended on the manual alignment of the two IDTs to produce an accurate SSAW and form an even distribution of PN and pressure anti-node lines. The  $S_{21}$  peak can be used to establish the angle of the IDTs, where the  $0^\circ$  angle achieves the maximum  $S_{21}$  peak as shown in Fig. 5A. The  $S_{11}$  of the transmitting IDT shows a dip of -28 dB when the two IDTs are in parallel (Fig. 5B), which is within an acceptable working range of conventional SAW devices<sup>25</sup>.

**Microchannel Characterisation**

Fig. 6A shows the average height and width of the 3D printed moulds, i.e.  $102.8 \pm 11.4 \mu\text{m}$  (Mean  $\pm$  SD) and  $451.4 \pm 42.6 \mu\text{m}$  (Mean  $\pm$  SD), respectively. Of which a  $500 \mu\text{m}$  wide 3D printed mould is used to produce the microchannel for the following tests (Fig. 6B). The bonding strength of the assembled microchannel met the high throughput requirement by flushing a sample at a flow rate of up to  $6 \text{ mL/min}$ <sup>26</sup>.

**Acoustic Energy Density within the VAD**

The acoustic energy density of the VAD at  $0^\circ$  is registered at 15, 20 and 27 dBm input power, as the results shown in Figs. 7A-7C, respectively. The time lapse required for 99% of microspheres to aggregate on the PN line is  $\sim 1.9$ ,  $\sim 0.6$ , and  $\sim 0.3$  sec for the three input powers. The average acoustic energy density of the powers is shown in Fig. 7D, which indicates that the acoustic radiation force exerted on the microspheres can be fully controlled by tuning the input power.

**Rotating the IDTs to Adjust the Tilted-Angle**

The VAD can offer reconfigurable tilted-angles (angle between the PN lines and the microchannel) without the need of fabricating new devices. The optimal tilted-angle degree in cell separation depends on the sample flow rate, where a high tilted-angle is optimal for the flow rate of  $25 \mu\text{L/min}$  and a low tilted-angle for  $50\text{-}125 \mu\text{L/min}$ <sup>6</sup>. The ability of VAD to vary the tilted-angle can potentially save considerable manufacturing effort and cost in reconfiguring devices for versatile and flexible applications. By simply rotating one of the IDTs, we manage to configure



the PN lines orientation into two tilted-angles,  $0^\circ$  and  $6^\circ$ , illustrated by the microsphere aggregation shown in Figs. 8A and 8B, respectively. The results demonstrate the ability of the VAD in rapid reconfiguration of the tilted-angle to tackle different applications.

### Visually Guided Assembly of the VAD

The VAD is tested for whether visually aligning the two opposite IDTs by eye can achieve similar performance as the VNA guided assembly. The VAD is assembled visually using the FSRs readings as reference. The alignment quality, represented by the  $S_{21}$ , is shown in Fig. 9A. Comparing with the VNA guided alignments (blue curve), the visually guided alignments (orange curve) present a smaller  $S_{21}$ . Fig. 9B shows the acoustic energy density is slightly higher in the visually guided assembly. This could be because the distance between the opposing IDTs may have been reduced during the visual experiments<sup>6</sup>. Since the IDTs are pushed further forward to expose their front edge and allow them to be easily visually aligned.

In addition, we collected the microsphere aggregation image for the visually guided assembly, as shown in Fig. 9C, which achieves a similar pattern as that in the VNA guided assembly (Fig. 8A). Overall, this confirms that the assembling process of the VAD can be achieved by the visual alignment of the two IDTs without the use of the VNA.

### Rotating the Microchannel

The unique construction of the VAD allows an alternative way to alter the tilted-angle by rotating the microchannel clamped to the VAD. New microchannel pressers are printed with two degrees including  $15^\circ$  and  $-5^\circ$  to accommodate a wider microchannel as shown in Fig. 10A. These pressers are utilised to clamp the microchannel and to create the respective inclinations for aggregating the microspheres, as shown in Fig. 10B.

It is noted that the reconfiguration of the tilted-angles can be achieved by either rotating the microchannel or the IDTs. It may be preferable to rotate the microchannel as it does not require to rotate the IDT, which may potentially affect the frequency response of the VAD.

## Conclusion

This paper introduced a novel technology to manufacture the SAW-based acoustofluidic system, including both the SAW IDT and the PDMS microchannel, without the need of a cleanroom facility. It was demonstrated that a pair of FPCB IDEs were mechanically coupled to the piezoelectric substrate to produce SSAWs, under the guide of either eyes or the VNA. The VAD offers great flexibility in resetting the tilted-angle between the IDTs and the microchannel, resulting in rotatable PN lines inside the acoustofluidic device. The VAD can accomplish a rapid acoustofluidic prototyping process as an alternative to the conventional cleanroom process.

## Acknowledgements

The authors would gratefully acknowledge the financial support from EPSRC (EP/P002803/1, EP/P018998/1), EPSRC IAA, Wellcome Trust, Global Challenges Research Fund (GCRF), the Royal Society (IEC\NSFC\170142, IE161019), and the Natural Science Foundation of China (NSFC) (Grant No. 51811530310).



References

1 Z. Tian, S. Yang, P.-H. Huang, Z. Wang, P. Zhang, Y. Gu, H. Bachman, C. Chen, M. Wu, Y. Xie and T. J. Huang, Wave number–spiral acoustic tweezers for dynamic and reconfigurable manipulation of particles and cells, *Science Advances*, 2019, **5**, eaau6062.

2 M. Wu, Z. Mao, K. Chen, H. Bachman, Y. Chen, J. Rufo, L. Ren, P. Li, L. Wang and T. J. Huang, Acoustic Separation of Nanoparticles in Continuous Flow, *Advanced Functional Materials*, 2017, **27**, 1606039.

3 M. Wu, Y. Ouyang, Z. Wang, R. Zhang, P.-H. Huang, C. Chen, H. Li, P. Li, D. Quinn, M. Dao, S. Suresh, Y. Sadovsky and T. J. Huang, Isolation of exosomes from whole blood by integrating acoustics and microfluidics, *Proc. Natl. Acad. Sci. U.S.A.*, 2017, **114**, 10584–10589.

4 M. Wu, C. Chen, Z. Wang, H. Bachman, Y. Ouyang, P.-H. Huang, Y. Sadovsky and T. J. Huang, Separating extracellular vesicles and lipoproteins via acoustofluidics, *Lab Chip*, 2019, **19**, 1174–1182.

5 Y. Gu, C. Chen, Z. Mao, H. Bachman, R. Becker, J. Rufo, Z. Wang, P. Zhang, J. Mai, S. Yang, J. Zhang, S. Zhao, Y. Ouyang, D. T. W. Wong, Y. Sadovsky and T. J. Huang, Acoustofluidic centrifuge for nanoparticle enrichment and separation, *Science Advances*, 2021, **7**, eabc0467.

6 P. Li, Z. Mao, Z. Peng, L. Zhou, Y. Chen, P.-H. Huang, C. I. Truica, J. J. Drabick, W. S. El-Deiry, M. Dao, S. Suresh and T. J. Huang, Acoustic separation of circulating tumor cells, *PNAS*, 2015, **112**, 4970–4975.

7 S. Li, L. Ren, P.-H. Huang, X. Yao, R. A. Cuento, J. P. McCoy, C. E. Cameron, S. J. Levine and T. J. Huang, Acoustofluidic Transfer of Inflammatory Cells from Human Sputum Samples, *Analytical Chemistry*, 2016, **88**, 5655–5661.

8 F. Guo, P. Li, J. B. French, Z. Mao, H. Zhao, S. Li, N. Nama, J. R. Fick, S. J. Benkovic and T. J. Huang, Controlling cell–cell interactions using surface acoustic waves, *PNAS*, 2015, **112**, 43–48.

9 D. Ahmed, A. Ozcelik, N. Bojanala, N. Nama, A. Upadhyay, Y. Chen, W. Hanna-Rose and T. J. Huang, Rotational manipulation of single cells and organisms using acoustic waves, *Nature Communications*, 2016, **7**, 11085.

10 J. Zhang, S. Yang, C. Chen, J. H. Hartman, P.-H. Huang, L. Wang, Z. Tian, P. Zhang, D. Faulkenberry, J. N. Meyer and T. J. Huang, Surface acoustic waves enable rotational manipulation of *Caenorhabditis elegans*, *Lab Chip*, 2019, **19**, 984–992.

11 L. A. Ambattu, S. Ramesan, C. Dekiwadia, E. Hanssen, H. Li and L. Y. Yeo, High frequency acoustic cell stimulation promotes exosome generation regulated by a calcium-dependent mechanism, *Commun Biol*, 2020, **3**, 553.

12 K. Xu, C. P. Clark, B. L. Poe, J. A. Lounsbury, J. Nilsson, T. Laurell and J. P. Landers, Isolation of a Low Number of Sperm Cells from Female DNA in a Glass–PDMS–Glass Microchip via Bead-Assisted Acoustic Differential Extraction, *Anal. Chem.*, 2019, **91**, 2186–2191.

13 R. J. Shilton, M. Travagliati, F. Beltram and M. Cecchini, Nanoliter-Droplet Acoustic Streaming via Ultra High Frequency Surface Acoustic Waves, *Advanced Materials*, 2014, **26**, 4941–4946.

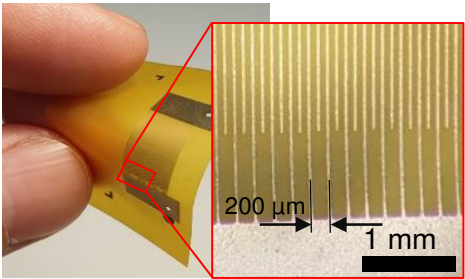
14 Y. Ai, C. K. Sanders and B. L. Marrone, Separation of *Escherichia coli* Bacteria from Peripheral Blood Mononuclear Cells Using Standing Surface Acoustic Waves, *Anal. Chem.*, 2013, **85**, 9126–9134.

15 N. Nama, R. Barnkob, Z. Mao, C. J. Kähler, F. Costanzo and T. J. Huang, Numerical study of acoustophoretic motion of particles in a PDMS microchannel driven by surface acoustic waves, *Lab Chip*, 2015, **15**, 2700–2709.

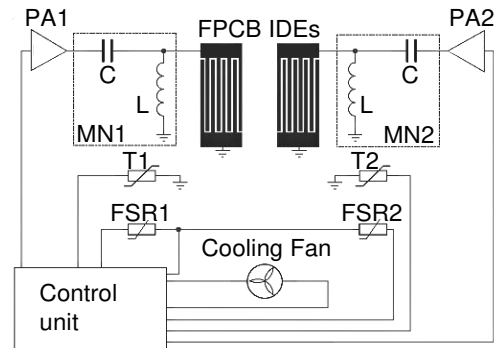
- 16 A. Ozcelik, J. Rufo, F. Guo, Y. Gu, P. Li, J. Lata and T. J. Huang, Acoustic tweezers for the life sciences, *Nature Methods*, 2018, **15**, 1021.
- 17 G. Liu, F. He, Y. Li, H. Zhao, X. Li, H. Tang, Z. Li, Z. Yang and Y. Zhang, Effects of two surface acoustic wave sorting chips on particles multi-level sorting, *Biomed Microdevices*, 2019, **21**, 59.
- 18 K.-A. Hyun, H. Gwak, J. Lee, B. Kwak and H.-I. Jung, Salivary Exosome and Cell-Free DNA for Cancer Detection, *Micromachines*, 2018, **9**, 340.
- 19 Y. Wang, C. Han and D. Mei, Standing Surface Acoustic Wave-Assisted Fabrication of Region-Selective Microstructures via User-Defined Waveguides, *Langmuir*, 2019, **35**, 11225–11231.
- 20 F. Guo, Z. Mao, Y. Chen, Z. Xie, J. P. Lata, P. Li, L. Ren, J. Liu, J. Yang, M. Dao, S. Suresh and T. J. Huang, Three-dimensional manipulation of single cells using surface acoustic waves, *PNAS*, 2016, **113**, 1522–1527.
- 21 T. D. Nguyen, V. T. Tran, Y. Q. Fu and H. Du, Patterning and manipulating microparticles into a three-dimensional matrix using standing surface acoustic waves, *Appl. Phys. Lett.*, 2018, **112**, 213507.
- 22 R. Mikhaylov, F. Wu, H. Wang, A. Clayton, C. Sun, Z. Xie, D. Liang, Y. Dong, F. Yuan, D. Moschou, Z. Wu, M. H. Shen, J. Yang, Y. Fu, Z. Yang, C. Burton, R. J. Errington, M. Wiltshire and X. Yang, Development and characterisation of acoustofluidic devices using detachable electrodes made from PCB, *Lab Chip*, 2020, **20**, 1807–1814.
- 23 C. Sun, R. Mikhaylov, Y. Fu, F. Wu, H. Wang, X. Yuan, Z. Xie, D. Liang, Z. Wu and X. Yang, Flexible Printed Circuit Board as Novel Electrodes for Acoustofluidic Devices, *IEEE Transactions on Electron Devices*, 2021, **68**, 393–398.
- 24 R. Barnkob, I. Iranmanesh, M. Wiklund and H. Bruus, Measuring acoustic energy density in microchannel acoustophoresis using a simple and rapid light-intensity method, *Lab on a Chip*, 2012, **12**, 2337–2344.
- 25 F. Wu, M. H. Shen, J. Yang, H. Wang, R. Mikhaylov, A. Clayton, X. Qin, C. Sun, Z. Xie, M. Cai, J. Wei, D. Liang, F. Yuan, Z. Wu, Y. Fu, Z. Yang, X. Sun, L. Tian and X. Yang, An Enhanced Tilted-Angle Acoustofluidic Chip for Cancer Cell Manipulation, *IEEE Electron Device Letters*, 2021, **42**, 577–580.
- 26 Y. Chen, M. Wu, L. Ren, J. Liu, P. H. Whitley, L. Wang and T. J. Huang, High-throughput acoustic separation of platelets from whole blood, *Lab Chip*, 2016, **16**, 3466–3472.

1  
2  
3  
4  
5  
6  
7  
8  
9  
10  
11  
12  
13  
14  
15  
16  
17  
18  
19  
20  
21  
22  
23  
24  
25  
26  
27  
28  
29  
30  
31  
32  
33  
34  
35  
36  
37  
38  
39  
40  
41  
42  
43  
44  
45  
46  
47  
48  
49  
50  
51  
52  
53  
54  
55  
56  
57  
58  
59  
60

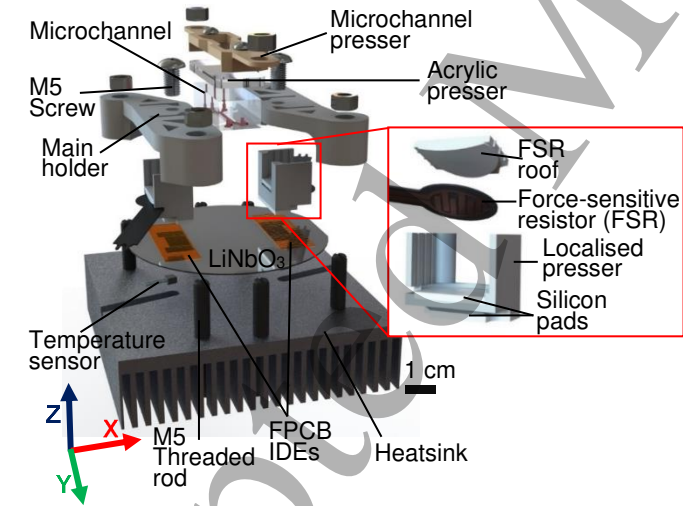
**FIGURE LIST**



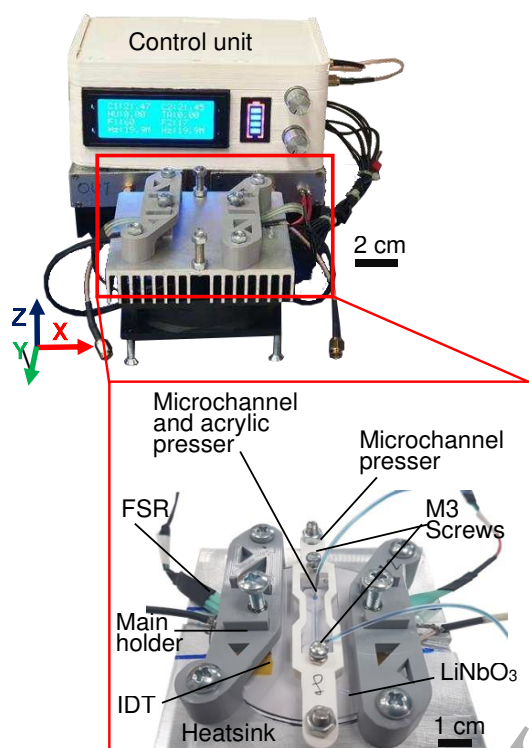
(A)



(B)

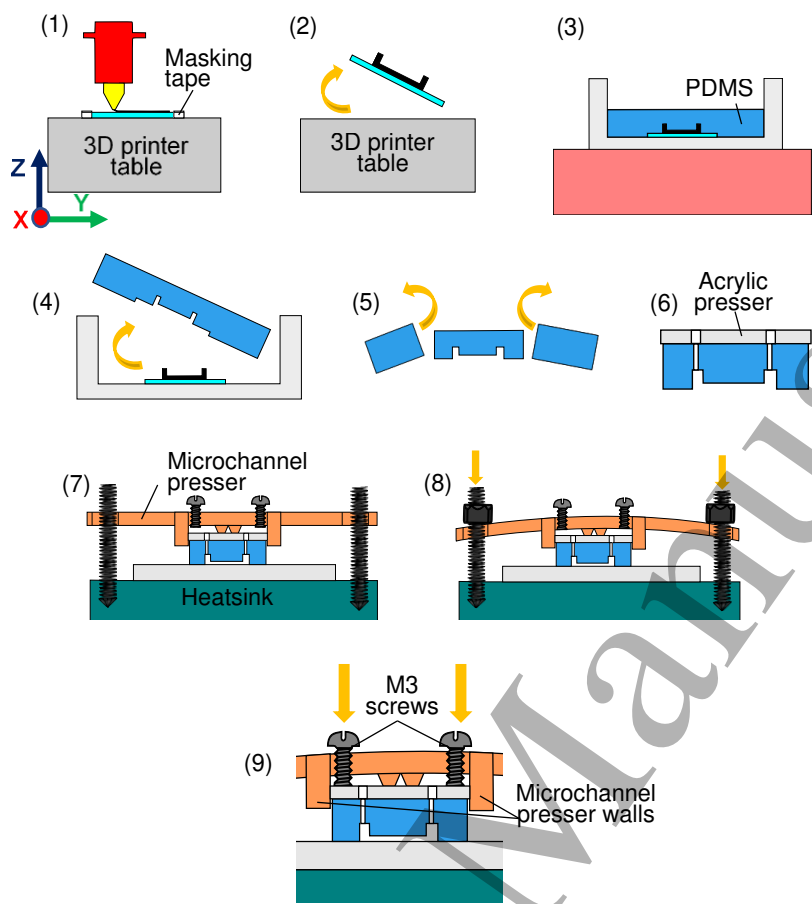


(C)

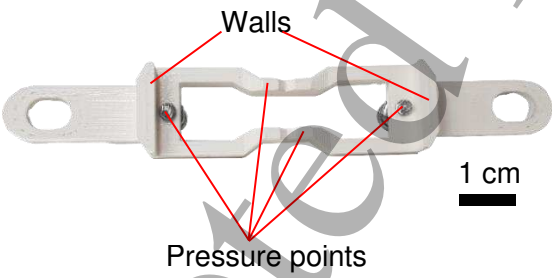


(D)

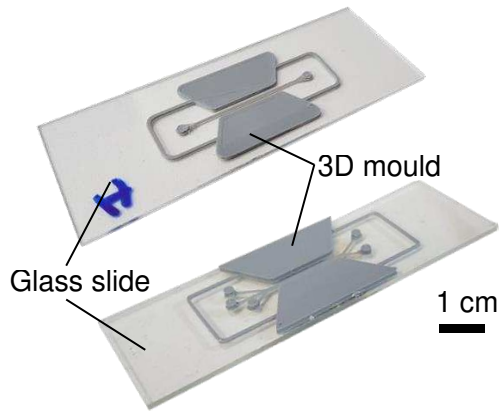
**Figure 1.** (A) Real-life flexible printed circuit board (FPCB) pre-patterned with interdigital electrodes (IDEs) with a zoom inset of the interdigital electrodes. (B) Schematic diagram of the Versatile Acoustofluidic Device (VAD) and a portable control unit, that can drive a cooling fan and provide radio frequency (RF) signals to drive the two IDTs. The RF signals are amplified by two 6W power amplifiers (PA1 and PA2). Each IDT is connected to a matching network (MN1 and MN2) for impedance matching. The values of the capacitor (C) and inductor (L) are 68 pF and 470 nH, respectively. The sensing components include two temperature sensors (T1 and T2) and force-sensitive resistors (FSR1 and FSR2). (C) 3D exploded view of the VAD with an inset presenting the assembly and components at the localised pressers. (D) The portable control unit and the VAD with an inset demonstrating the real-life model of the assembled VAD on the heatsink.



357 (A)



358 (B)



359 (C)

360 **Figure 2.** (A) The development steps of the microchannel using the glass-bottom 3D printed  
361 mould. (B) The microchannel presser with its the pressure points and walls highlighted. (C) Real-  
362 life models of the glass-bottom 3D printed mould.

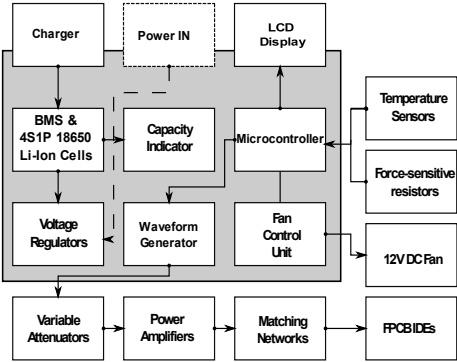


**Figure 3.** The respective block schematic demonstrating all the internal and external components of the control unit.



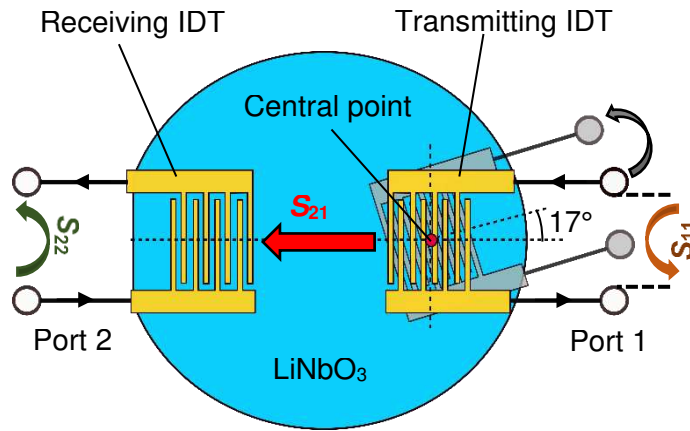


**Figure 4.** IDT rotation test for investigating the use of the vector network analyser (VNA) to register the alignment of the IDTs. The transmitting IDT being rotated around its central point, while the receiving IDT is held fixed.

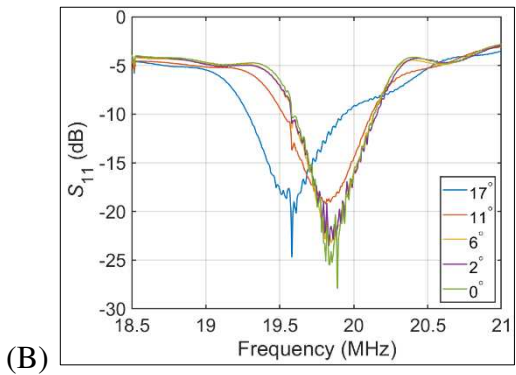
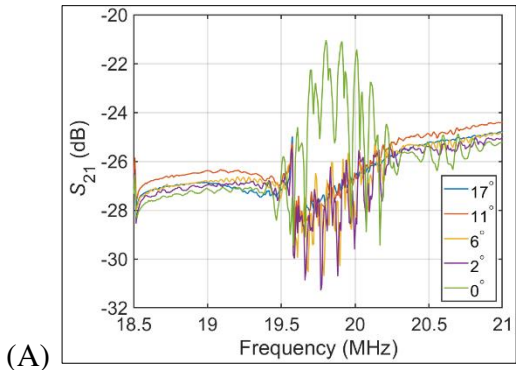
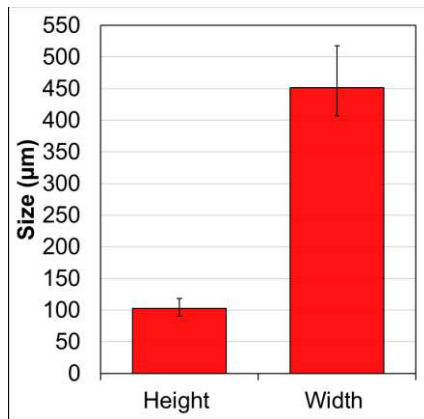
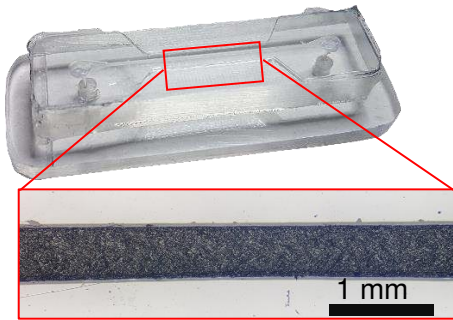


**Figure 5.** *S*-parameters of the VAD during the rotation of one IDT. (A) Average insertion loss ( $S_{21}$ ) for each different angle during the rotation. (B) Average reflection coefficient ( $S_{11}$ ) for each different angle during the rotation.



(A)



(B)

**Figure 6.** (A) The 3D printed mould's average height and width of  $102.8 \pm 11.4 \mu\text{m}$  (Mean  $\pm$  SD) and  $451.4 \pm 42.6 \mu\text{m}$  (Mean  $\pm$  SD), respectively. (B) Real-life model of a  $500 \mu\text{m}$  wide microchannel sitting on top of the acrylic presser.

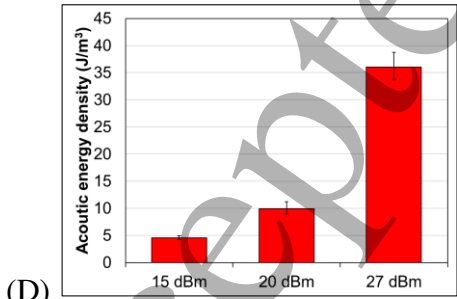
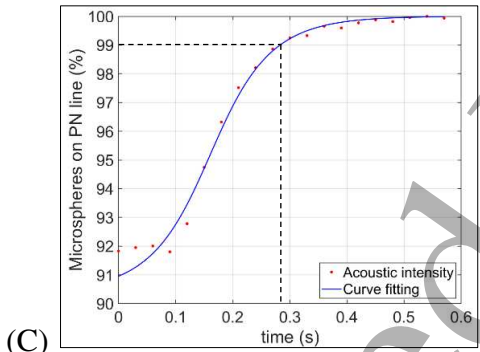
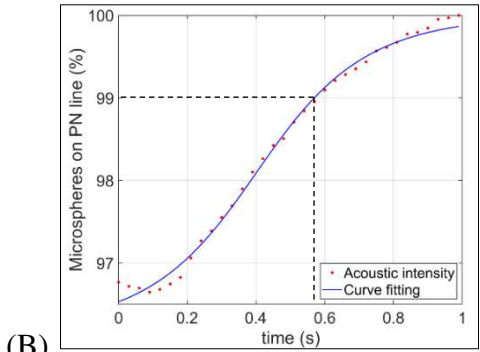
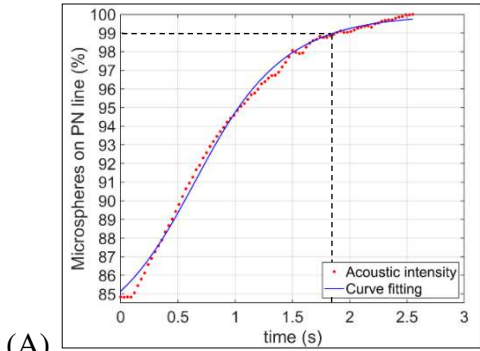
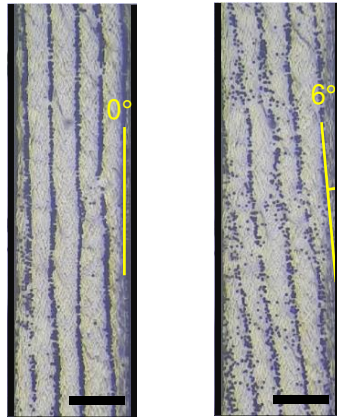


**Figure 7.** Acoustic energy density of the VAD with parallel IDTs. (A)-(C) Under the input power of 15 dBm, 20 dBm, and 27 dBm, the time for 99% of microspheres to reach the PN line is ~1.9, ~0.6, and ~0.3 sec, respectively. (D) The average acoustic energy densities for the three input powers are 4.6, 9.9, and 36  $\text{J/m}^3$ , respectively ( $n = 3$ ).



(A) (B)

**Figure 8.** Microscope images showing the reconfigurability of the VAD in setting the PN lines to (A)  $0^\circ$  and (B)  $6^\circ$ . The microspheres are aggregated on the PN lines exhibiting the angle against the wall of the microchannel. (200  $\mu\text{m}$  scale bar)

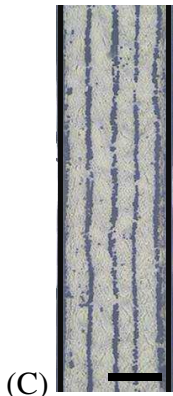
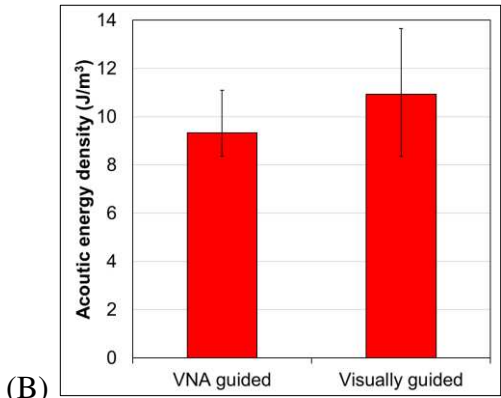
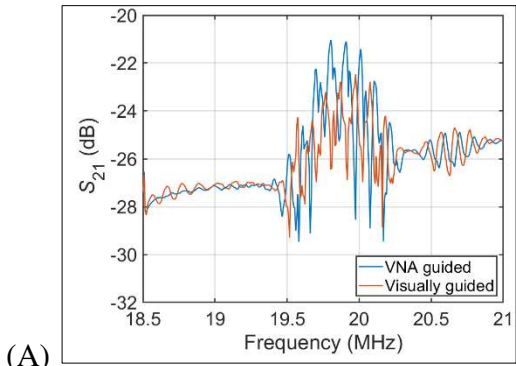


**Figure 9.** (A) The  $S_{21}$  of the VAD assembled using the VNA and the visually guided assembly of the two IDTs. ( $n = 5$ ) (B) Acoustic energy density of the VAD constructed by the two assembly methods, VNA and visually, with an acoustic energy of  $9.3 \pm 1.2 \text{ J/m}^3$  (Mean  $\pm$  SD) and  $10.9 \pm 2.7 \text{ J/m}^3$  (Mean  $\pm$  SD), respectively. ( $n = 3$ ) (C) Microsphere aggregation on the PN lines of the VAD constructed by visually guided assembly ( $200 \mu\text{m}$  scale bar).

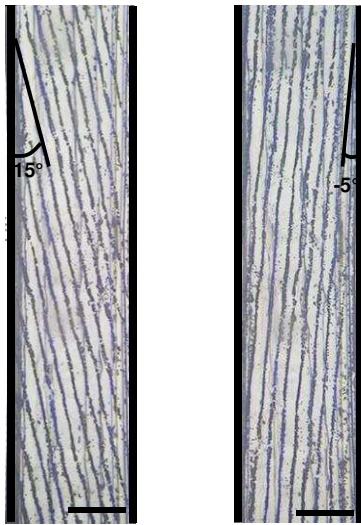
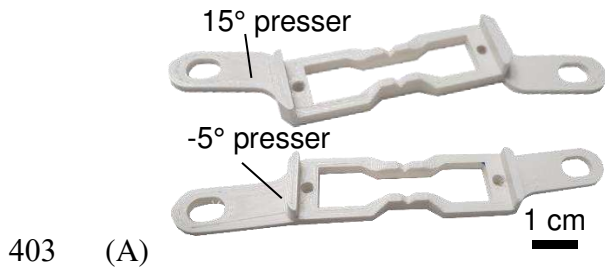


**Figure 10.** Rotating the microchannel to a set tilted-angle. (A) 3D printed 15° and -5° microchannel pressers. (B) Aggregated microspheres on the PN lines of 15° (left) and -5° (right) angles, in regard to the microchannel wall (450  $\mu\text{m}$  scale bar).